IEEE Access
Multidisciplinary ⋮ Rapid Review ⋮ Open Access Journal

Received 2 July 2023, accepted 13 August 2023, date of publication 17 August 2023, date of current version 23 August 2023.

Digital Object Identifier 10.1109/ACCESS.2023.3305993

RESEARCH ARTICLE

Study on the Pressure Field Reconstruction Method and Its Relationship With Audible Noise of DC Corona Discharge

MENG WEI[1,2], LI LI[1], LI QI[2,5], LI DUANJIAO[3], HU JIANLIN[2], (Member, IEEE), WANG HONGBIN[4], ZHENG XIAOGUANG[1], AND ZHONG WANLI[1]

[1]Key Laboratory of Environmental Protection of Guangdong Power Grid Co., Ltd., Electric Power Research Institute of Guangdong Power Grid Co., Ltd., Guangzhou, Guangdong 510080, China
[2]Xuefeng Mountain Energy Equipment Safety National Observation and Research Station, Chongqing University, Chongqing 400044, China
[3]Guangdong Power Grid Company Ltd., Guangzhou, Guangdong 510600, China
[4]Guangzhou Power Supply Bureau, Guangdong Power Grid Company Ltd., China Southern Power Grid, Guangzhou 510620, China
[5]Department of Electrical and Electronic Engineering, The University of Manchester, M13 9PL Manchester, U.K.

Corresponding authors: Meng Wei (20161102063t@alu.cqu.edu.cn) and Li Qi (qi.li@cqu.edu.cn)

This work was supported by Electric Power Research Institute of Guangdong Power Grid Co., Ltd., under Grant 036100KK52200034(GDKJXM20201968).

ABSTRACT DC corona audible noise (AN) is one of the electromagnetic interference from power grids and the key factors affecting the electrical design of power transmission and distribution equipment. The measurement method is crucial to study the generation mechanism of audible noise. This paper proposed a Schlieren optical measurement with a corresponding numerical reconstruction method to measure the audible noise within DC corona discharge and quantified it with the pressure field. Numerical experiments are conducted to verify the accuracy of the pressure field re-construction method. The relationship between the pressure field and sound pressure during DC corona discharge is experimentally studied. Results show that the reconstruction error is within 5%; the Schlieren system captures the gas expansion process and pressure field in the discharge region at the microsecond timescale. During corona discharge, the radial radius of the discharge region increases while its pressure decreases and overpressure increases. A relationship of non-linear proportional increase appears between the pressure field and audible noise, and only a small portion of the pressure field is converted into audible noise. The new method demonstrated in this paper is an effective way of measuring and analyzing the pressure field in the DC corona discharge, which would be the key to understanding the mechanism of acoustic wave (or AN) generation from DC corona discharge on transmission lines.

INDEX TERMS Schlieren method, electromagnetic interference, pressure field reconstruction, dc corona, audible noise measurement.

I. INTRODUCTION

The audible noise of DC corona discharge will directly affect the daily life of residents near the transmission lines and substations [1], [2], [3]. The resulting environmental assessment and noise complaints have brought difficulties to the operation and maintenance of power transmission and transformation facilities [4], [5], [6]. Establishing a set of measurement and reconstruction methods for the pressure field of the corona discharge region plays a vital role in revealing the mechanism of audible noise and guiding the corona effect evaluation and electrical design of power transmission and transformation equipment.

The audible noise generated by corona discharge is a mechanical wave [7]. Its primary measurement method is the same as that of environmental acoustics [7]. Re-searchers use the sound pressure probe to measure the time domain waveform of sound pressure to obtain the sound pressure level or directly use the sound level meter to measure the weighted sound level. In recent years, researchers have used these two methods to study the time-frequency domain characteristics of DC transmission lines, single point, and multipoint corona

The associate editor coordinating the review of this manuscript and approving it for publication was Enamul Haque.

audible noise, and obtained the influence of the external insulation environment on corona audible noise characteristics [8], [9], [10], [11], [12], [13]. It is found that there is a one-to-one correspondence between the waveform of DC corona audible noise and the current in the time domain [14]. The audible noise waveform generated by positive and negative corona is the bipolar pulse. The noise pulse is in the form of a positive half-wave first and connects with a negative half-wave in the time domain. The positive half-wave comes from gas compression, and the negative half-wave comes from gas expansion [15]. In the existing research, the audible noise measurement measures the acoustic pulse directly through the sound pressure sensor at a certain distance from the corona source, and calculates the weighted sound level, sound power, and other acoustic characteristic parameters. This method is the most commonly used and mature in acoustics. However, its accuracy depends on the sound field environment and test layout when measuring the sound waves generated by corona discharge in space. The actual test has high requirements for the acoustic performance of the laboratory [16]. For this reason, Manchester University [10] built an artificial anechoic chamber to construct a semi-free sound field to isolate low-frequency vibration and the interference caused by the partial discharge of the high-voltage power supply. North China Electric Power University [17] proposed a set of methods to eliminate sound refraction and background noise interference to improve the accuracy of measurement results. Although these methods perform well in the measurement, they are technically complex in the hardware and software, which limits their popularization and practicality, making it challenging to eliminate interference in the measurement of corona noise. In addition, the acoustic sensor needs to be far away from the corona source, which makes it difficult for researchers to establish the relationship between audible noise and corona characteristics at the micro level, which brings difficulties in studying the mechanism of corona audible noise.

During DC corona discharge, electrons transfer kinetic energy to gas molecules through collision and store it in rotation, translation, excitation, ionization, dissociation, and vibration energy. The increase of translational kinetic energy will directly increase the temperature of gas molecules in the corona discharge area, increasing the gas pressure and density and then decreasing with the gas's expansion in the discharge area [18]. In this process, the molecular displacement caused by the change of gas density in the discharge area will diffuse to the outside in the form of waves, thus forming sound waves. Therefore, the pressure change in the corona discharge area can be reflected by measuring the gas density change in the corona discharge area, and the audible noise generated by the corona discharge can be analyzed. Gladstone-Dale law points out that gas density is proportional to its refractive index difference [19]. Currently, the methods for measuring the refractive index of gas include optical interferometry, optical fiber method, microwave resonance method, and optical deflection method. The Schlieren method based on the optical deflection principle can directly obtain the density information through the deflection angle of the Schlieren image while meeting the non-contact measurement requirements during gas discharge [20]. Its measurement accuracy and spatial resolution depending on the lens parameters and image-receiving device [20]. Thus, the Schlieren method is particularly suitable for measuring gas discharge phenomena with weak luminescence and small sizes, such as long gap streamer [21], leader discharge [22], and faraday area of glow discharge [23]. However, the existing research on the Schlieren image and its numerical analysis technology mainly focuses on the gas temperature in the discharge area [23], [24]. For corona discharge with gas temperature maintained near room temperature, there are few studies on its density and pressure field.

This paper set up a Schlieren system to measure the density of the corona discharge region based on the principle of gas translational energy transfer and light deflection. A reconstruction method for the pressure field in the corona discharge region is proposed, and numerical experiments verify the accuracy of this method. Finally, the Schlieren image and the reconstruction effect of the pressure field measured in corona discharge to spark discharge are given and the relationship between sound pressure and pressure field are experimentally studied. The Schlieren optical system and the numerical methods of this paper are suitable for the experiment study in the laboratory, the research results can provide a technical basis and a new measurement method for investigating the mechanism of the audible noise emitted from corona discharge.

II. PRINCIPLE FOR AUDIBLE NOISE MEASUREMENT (QUANTIFIED BY PRESSURE FIELD) AND IMAGE PROCESSING METHOD OF CORONA DISCHARGE

A. PRINCIPLE OF SCHLIEREN METHOD FOR MEASURING THE DENSITY OF CORONA DISCHARGE REGION

Based on Gladstone – Dale law (see equation 7), this paper quantitatively reflects the corona discharge area's density by measuring the refractive index. The Schlieren system indirectly measures its refractive index through the light deflection angle of the discharge area [25], [26], [27], [28]. As shown in Figure 1, it is the basic schematic diagram of Schlieren imaging and deflection angle measurement using the light deflection property of the discharge area.

The green detection light in Figure 1 passes through the discharge area and is received by the camera to form discrete deflection angle data α. These deflection angles are the line integral of the detection light along the x-axis direction of the discharge area. The relationship between the deflection angle of the discharge area and the refractive index is shown in equation (1) [17]:

$$\alpha(y) = \frac{2y}{n_0} \int_y^R \frac{\partial n(r)}{\partial r} \cdot \frac{1}{\sqrt{r^2 - y^2}} \cdot dr \tag{1}$$

where R represents the border radius of the discharge region, r represents the radial distance, the Abel inversion equation

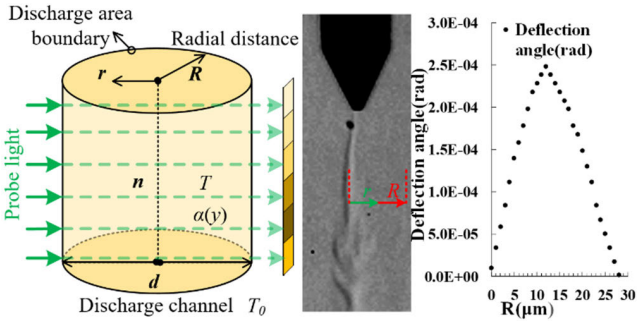

FIGURE 1. Schematic diagram of schlieren measurement.

of equation (1) is:

$$n(r) = -\frac{1}{\pi}\int_r^R \alpha(y)\cdot\frac{dy}{\sqrt{y^2-r^2}} + n_0 \tag{2}$$

where n_0 is the background refractivity, $n(r)$ is the radial distribution of the refractivity, $\alpha(y)$ represents the obtained deflection angle. According to the deflection angle information in the Schlieren image, the discharge region's refractivity can be calculated by equation (2).

This paper uses the linear Schlieren optical path, which is one of the most straightforward and practical Schlieren optical paths. In contrast, the calibration lens is used to improve the imaging results, as shown in Figure 2.

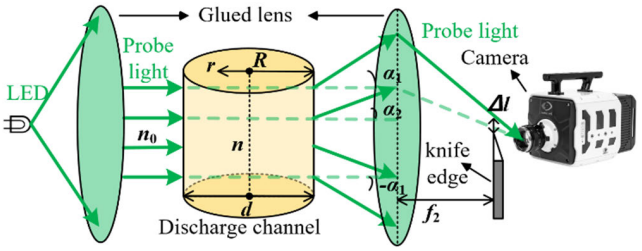

FIGURE 2. Schematic diagram of schlieren system.

The imaging device consists of a Schlieren system and a Phantom V710Ls high-speed camera. The Led lamp generates a 532nm green probe light. After the primary condenser lens with a focal length of 15cm converges, the light source's image with clear edges is generated through a small hole. Then, two glued lenses with a focal length of 25cm are used to form parallel light and pass through the discharge area. The spatial resolution is 10∼100μm/pixel adjustable, and the time resolution is 1∼38.45 μS adjustable. The image passes through a filter (central wavelength 532nm ± 10nm, transmissivity>75%) and is focused at the knife edge to achieve quantitative measurement of the deflection angle. The camera directly obtains the gray level change of the discharge area. The quantitative relationship between the gray level and deflection angle can be obtained through a concave lens (calibration lens) with a known refractive index, as shown in Figure 3.

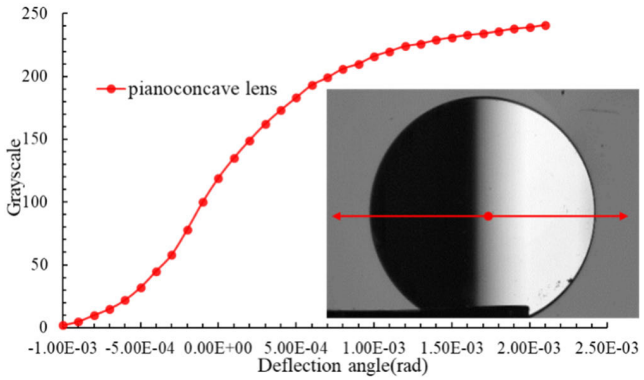

FIGURE 3. Quantitative curve of gray scale and deflection angle.

After the Schlieren image is measured, the grayscale is converted into the deflection angle by comparing it with Figure 3. Then the refractive index of the discharge area can be obtained by substituting it into equation (2).

B. SCHLIEREN IMAGE PROCESSING METHOD

During measurement, the camera captures the scattered gray points in the dis-charge area. The dispersion degree of the scattered points depends on the camera's resolution, the geometric size of the discharge area, and stability. The stability of the discharge area depends on the energy exchange between the discharge area and the outside. Figure 4 shows the Schlieren image of the corona and spark discharge.

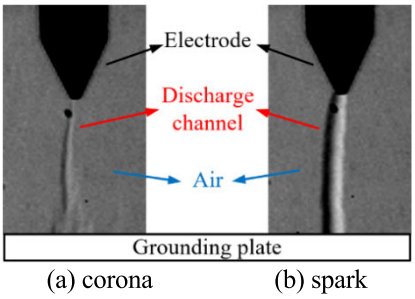

FIGURE 4. Schlieren images of corona and spark.

Figure 4 shows that the corona discharge has a small geometric size, relatively stable channel shape, and small gray level change. The spark discharge has a sizeable geometric size and significant grayscale change. This difference determines that different image processing methods should be used for corona and spark discharge areas.

1) IMAGE PROCESSING METHOD OF CORONA DISCHARGE AREA

Due to the low gas temperature in the corona discharge area, there is no apparent thermal expansion, and the size of the discharge area is minimal. Figure 5 shows the original deflection angle points in the corona discharge area and the deflection angle interpolated by different image processing methods.

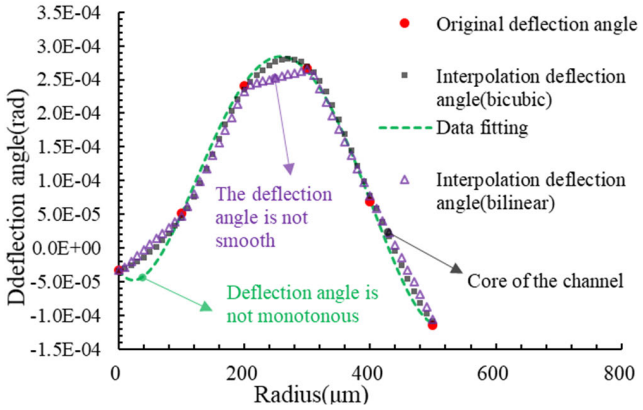

FIGURE 5. Deflection angle of brush discharge channel.

As shown in Figure 5, the red circular scatter points are the discharge area's original deflection angle. It can be seen that the axial position of the discharge area cannot be directly found through the original deflection angle points (deflection angle is 0), and the scatter points only show the outline of the discharge area. Purple triangle, gray square, and green dotted line are the results obtained by bilinear interpolation, bicubic interpolation, and curve fitting, respectively. It can be seen from the figure that bilinear interpolation has uneven interpolation points due to fewer original deflection angle sampling points. At the same time, the deflection angle would be more varied in the curve fitting method. The bicubic interpolation can directly determine the axis of the discharge region to ensure the deflection angle's monotony and smoothness.

2) IMAGE PROCESSING METHOD OF THE SPARK DISCHARGE REGION

The temperature of the spark discharge area is higher than that of the corona, and the heat exchange with the external environment is more substantial than the corona. Hence, the region has more sampling points and poor distribution regularity. Figure 6 shows the deflection angle of the spark discharge area.

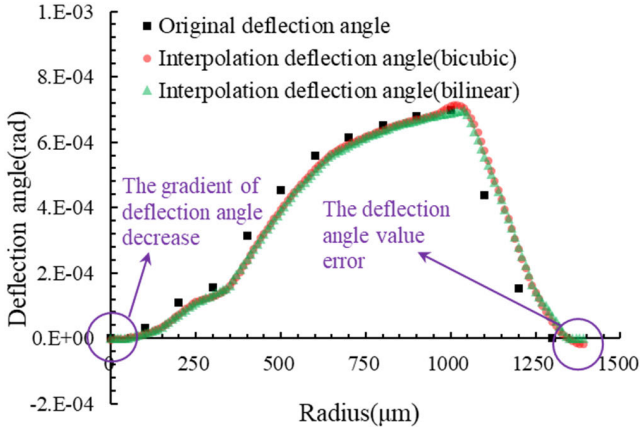

FIGURE 6. Deflection angle of spark discharge channel.

As shown in Figure 6, the black square points are the original deflection angle in the spark discharge area. The circular red point is the deflection angle obtained by bicubic interpolation; green triangle points are deflection angles by bilinear interpolation. When there are many original sampling points near the axis, and the distribution regularity is poor, the interpolation would lead to the decline of the deflection angle gradient. At the region's boundary, there is a numerical error that the deflection angle is less than 0. Therefore, when calculating the spark discharge area, the original deflection angle points of the region are directly used for calculation instead of image interpolation.

III. CORONA PRESSURE FIELD RECONSTRUCTION METHOD AND NUMERICAL EXPERIMENT

A. RECONSTRUCTION METHOD OF REFRACTIVE INDEX FIELD IN DISCHARGE REGION

After the deflection angle of the discharge area is obtained, the corresponding refractive index can be calculated by bringing it into equation (2). The integral limit of the independent variable in equation (2) is $r \sim R$, which means the integral is from the radial r to the boundary of the discharge region. Therefore, at each calculation point, when y=r in the radial direction, there is $1/(y^2\text{-}r^2)^{0.5} = \infty$, which means each calculation point of equation (2) is a singular point, and its analytical solution is impossible. In order to solve equation (2), a numerical calculation method must be used. At the same time, the existence of singular points makes the numerical integration methods with trapezoidal, rectangular, and Simpson forms invalid. Therefore, based on the existing Guss-Legendre integration equation, this paper proposes a linear approximation method to solve the singular point problem at the axis of the discharge region. Firstly, the integral interval [r, R] is reconstructed by a linear transformation, as shown in equation (3).

$$y = \frac{(R-r)}{2} \cdot t + \frac{(R+r)}{2} \tag{3}$$

The integral interval $y \in [r, R]$ can be transformed into $t \in [1, -1]$ by equation (3). From the definite integral transformation integration method, we can get:

$$\int_r^R f(y)dy = \frac{(R-r)}{2} \cdot \int_{-1}^{1} f\left(\frac{(R-r)}{2}t + \frac{(R+r)}{2}\right)dt \tag{4}$$

Further use the Guass-Legendre equation to construct the discrete form of equation (4):

$$\int_{-1}^{1} f(t)dt \approx \sum_{k=0}^{N} [A_k \cdot f(t_k)] \tag{5}$$

where A_k is the quadrature coefficient: $A_k = (R\text{-}r)/2$. It can be seen from equations (4) and (5) that after the integral interval $[r, R]$ is discrete, the function value $f(r)$ of $[r, r]$ at the singular point is actually set to 0 by the quadrature coefficient $A_k = (r\text{-}r)/2$. Finally, the value of the singular

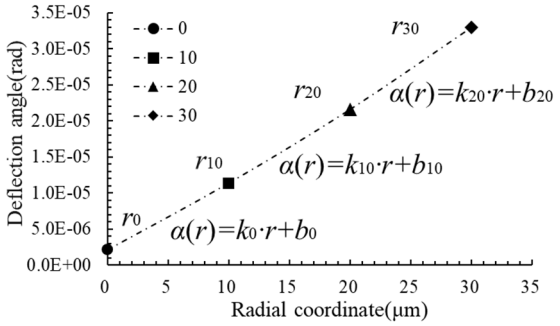

FIGURE 7. Schematic diagram of linear approximation method.

point is approximated by increasing the number of discrete intervals N. In this paper, the linear fitting method is used further to construct the discrete region near the singular point to achieve the goal of controllable approximation accuracy. Take the deflection angle point, as shown in Figure 7.

The scattered data points shown in Figure 7 are discrete points of deflection angle whose radial coordinates and deflection angle are known. The linear Equation between these two points can be constructed from the two adjacent points $\alpha(r) = kr+b$. Taking the points r_0 and r_{10} in Figure 7 as examples, the linear Equation is:

$$\alpha\,(r) = \frac{(\alpha_{10} - \alpha_0)}{(r_{10} - r_0)} \cdot r + \alpha_0 \tag{6}$$

Since the deflection angle and radial coordinates of the points r_0 and r_{10} are known, the linear Equation can be directly solved. At this time, the deflection angle of the point r_0+dr near the singular point r_0 can be directly calculated according to the linear equation $\alpha(r_0+dr)$. The singular point problem caused by $1/(y^2\text{-}r^2)^{0.5} = \infty$ can be avoided when the point r_0+dr is used to replace the point r_0+dr in equation (2). Since the Equation of the replacement point r_0+dr is known, the calculation accuracy can be manually controlled by setting the value of dr.

B. PHYSICAL MODEL OF PRESSURE FIELD IN CORONA DISCHARGE REGION

The physical model is necessary to calculate the pressure in the corona discharge region. The gas constant model is often used for corona discharge with the gas temperature at room temperature. The basic principle of the gas constant model is that when the temperature, molar mass, and Gladstone-Dale constant of the gas are constant, the gas density and the difference in the gas refractive index obey a clear functional relationship. The gas density can be calculated by measuring the difference in the gas refractive index. The plasma generated by air discharge at atmospheric pressure is a conductive gas. Its pressure, volume, amount of material, and gas temperature meet the ideal gas law, and the optical refractive index and gas density meet the Gladstone-Dale Relation. This paper first deduces the relationship between gas temperature and refractive index from the universal law of gas. When a beam of light with a specific wavelength passes through the gas, the Gladstone-Dell relationship points out that the relationship between the refractive index of gas and its density follows equation (7):

$$\gamma - 1 = K_{\mathrm{G}} \cdot \rho \tag{7}$$

where γ represents the refractive index, γ-1is the specific refractive index, ρ reprecents the gas density, kg/m^3; K_{G} is the Gladstone-Dell constant, m^3/kg; K_{G} depends on the particle components and the probe light wavelength, K_{G} could be calculated by equation (8)

$$K_{\mathrm{G}} = \frac{\left(e^2 \cdot L_{\mathrm{os}}\right)}{\left(2\pi \cdot c^2 \cdot m_{\mathrm{e}} \cdot M\right)} \sum \frac{\left(f_{\mathrm{i}} \cdot \lambda_{\mathrm{i}}^2 \cdot \lambda\right)}{\left(\lambda^2 - \lambda_{\mathrm{i}}^2\right)} \tag{8}$$

where e is the electron charge, C; L_{os} represents the Loschmidt number, m^{-3};c represents the light speed in the vacuum, m/s; m_{e} is the mass of electron, kg;M is the mole mass of the gas, g/mol; f_{i} is the resonance intensity of various molecules in the gas, λ_{i} is the resonant wavelength of various molecules in the gas, nm; λ represents the wavelength of the probe light, nm.

It can be seen from equation (8) that the change of particle type in the gas and detection light wavelength will cause a change in K_{G}. When the light of a single wavelength is used to measure gas, K_{G} depends on the composition of particles in the gas. Calculate the gas density in Equation (7) according to the ideal gas law, as shown in Equation (9).

$$\rho = \frac{(M \cdot P)}{\left(R_{\mathrm{con}} \cdot T_{\mathrm{gas}}\right)} \tag{9}$$

where M is the molar mass of the gas, g/mol; P represents the gas pressure, Pa; R_{con} is the general gas constant, J/(K·mol); T_{gas} is the gas temperature, K. take the equation (9) into (7), the relationship between pressure P_{gas} and specific refractive index γ-1 could be described by equation (10):

$$P_{gas} = \frac{\left[T_{gas} \cdot R_{\mathrm{con}} \cdot (\gamma - 1)\right]}{(K_G \cdot M)} \tag{10}$$

where the general gas constant R_{con} is independent from the gas species.

Assuming that the molar mass, gas pressure, gas temperature, refractive index difference, and Gladstone-Dale constant of the gas from t_0 to t_1 have changed, the relationship between the gas parameters at t_0 and t_1 is shown in equation (11).

$$\frac{P_{\mathrm{gas1}}}{P_{\mathrm{gas0}}} = \frac{(\gamma_1 - 1)}{(\gamma_0 - 1)} \cdot \frac{(K_{\mathrm{G0}} \cdot M_0)}{(K_{\mathrm{G1}} \cdot M_1)} \cdot \frac{T_{\mathrm{gas1}}}{T_{\mathrm{gas0}}} \tag{11}$$

The text 0 and 1 represents the t_0 moment and t_1 moment.

Equation (11) establishes the relationship between the gas temperature and the molar mass, gas pressure, gas temperature, refractive index, and Gladstone-Dale constant of the gas at different times. When the gas temperature is unchanged, the air's molar mass, gas pressure, and Gladstone-Dale constant will remain unchanged. Thus, Equation (11) can be

simplified as the relationship between the gas temperature and refractive index, as shown in Equation (12).

$$\begin{cases} P_{\text{gas1}} = \frac{(\gamma_1 - 1)}{(\gamma_0 - 1)} \cdot P_{\text{gas0}} \\ P_{dgas} = P_{\text{gas0}} - P_{\text{gas1}} \end{cases} \tag{12}$$

According to Equation (12), the gas pressure P_{gas0} and refractive index γ_0 at the time t_0 are known. By measuring the refractive index γ_1 of the gas at time t_1, the gas pressure at time t_1 can be calculated directly. According to equation (2), the Schlieren method measures the refractive index of gas γ. Therefore, by continuously recording a group of Schlieren images, the pressure change of the gas can be calculated according to equation (12). Finally, the over pressure P_{dgas} can be calculated using P_{gas0} minus P_{gas1}.

According to the equation (11), there is $M_0 \approx M_1$, $K_{\text{G0}} \approx K_{\text{G1}}$, and $T_0 \approx T_1$ when the variation of M, K_{G}, and T could be ignored compared with specific refractive index γ-1. Thus, the pressure of the discharge region P_{gas1} and the over pressure P_{dgas} could be calculated by equation (12).

C. VERIFICATION OF PRESSURE FIELD RECONSTRUCTION ACCURACY

The accuracy of the pressure reconstruction method depends on the accuracy of the Abel inversion algorithm. The simplest way to verify the Abel inversion algorithm is to compare the known refractive index distribution with the reconstructed one. The current research results show that the density, temperature, and current distribution in the gas discharge under atmospheric pressure are close to normal distribution [29], [30], [31], [32]. Therefore, this paper uses the standard function to build a simulated refractive index to verify the accuracy of the Abel inversion algorithm. The verification is carried out in the following steps:

1) The standard deviation is 0.1618 (shape parameter), and the mean value is 0 (position parameter). The following equation (13) is used to build the simulated refractive index distribution function in the discharge area.

$$\gamma\,(r)_{moni} = n_0 - \left[\frac{1}{\left(\sqrt{2\pi} \cdot \sigma_{moni}\right)} \cdot e^{-\frac{(r-\mu_{moni})}{(2\cdot\sigma^2_{moni})}} \right] \cdot 10^{-4} \tag{13}$$

where, the subscript moni represents the simulated discharge area refractive index function, σ_{moni}, μ_{moni} is the shape and position parameters, respectively. n_0 is the background refractive index of air, r is the radial coordinate.

2) equation (13) is introduced into equation (1) to calculate the Abel positive transformation to obtain the simulated deflection angle distribution in the discharge area, and equation (12) is substituted to calculate the simulated pressure distribution;

3) The simulated deflection angle is resampled, and the number of sampling points can be selected manually;

4) The Abel inverse conversion method is used to calculate the sampled deflection angle points to obtain the reconstructed refractive index distribution, and the reconstructed pressure distribution is calculated by substituting it into equation (12);

5) The reconstructed pressure distribution is compared with the original pressure distribution to verify the algorithm's accuracy.

Figure 8 shows the schematic diagram of the sampling points used to simulate the deflection angle in this paper. The radial coordinates in the diagram use normalized values. It can be seen from the black curve that the gradient of the simulated deflection angle near the axis center is the largest. The deflection angle increases linearly with the increase of the radial distance within the range of 0∼0.1. The deflection angle changes gently when the radial distance is greater than 0.1.

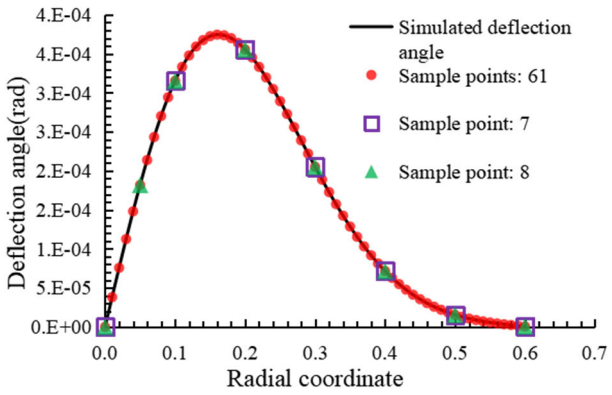

FIGURE 8. Schematic diagram of deflection angle simulation distribution and sampling points.

This paper samples 61 points of simulated deflection angle in 0.01 step size, 7 points with the step size of 0.1, and based on the step size of 0.1, one more sampling point is added in the radial range of 0∼0.1. The specific refractive index is reconstructed using these sampling points. Take 61, 7, and 8 sampling points as the input points, respectively, bring them into equation (2), calculate the refractive index distribution using the refractive index field reconstruction method proposed in this paper, and then substitute them into equation (12) to calculate the pressure distribution. The obtained pressure reconstruction results and the original simulated pressure distribution curve are shown in Figure 9.

As shown in Figure 9, the solid black line, red dot, purple box, and yellow triangle are the simulated pressure distribution and the pressure reconstruction results, respectively. It can be seen from the figure that the reconstructed pressure is in good agreement with the original curve using 61 sampling points. The pressure at the axis is smaller and larger at the radial of 0.1 than the original pressure under seven sampling points. The reconstructed pressure performs much better under eight sampling points compared with seven. The accuracy of the pressure reconstruction method and its influencing factors are analyzed quantitatively by comparing the relative error between the reconstructed pressure and the original one, as shown in Figure 10.

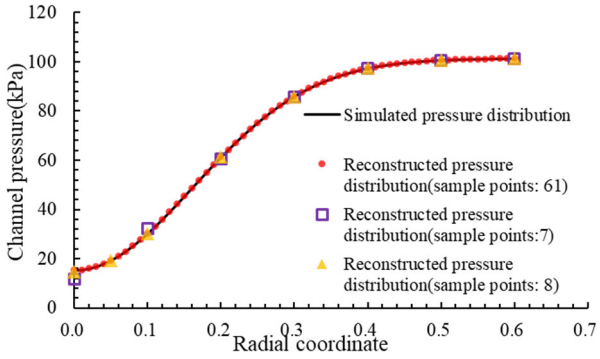

FIGURE 9. Schematic diagram of pressure simulation distribution and reconstruction results.

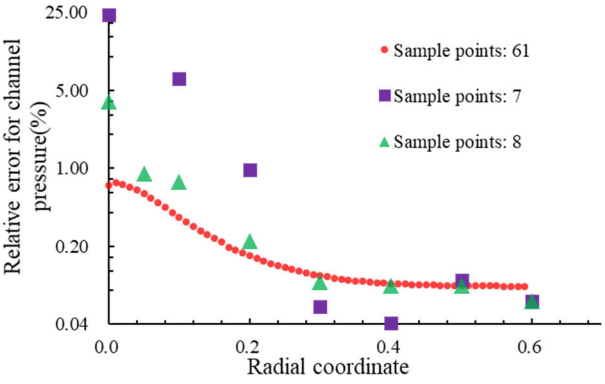

FIGURE 10. Schematic diagram of pressure reconstruction error at different sampling points.

Figure 10 shows the pressure reconstruction error under different sampling points. The red dot, purple square, and green triangle are reconstruction errors under 61, 7, and 8 sampling points, respectively. Under 61 sampling points, the relative error of the reconstructed pressure is within 1%, and the maximum error (about 0.7%) occurs at the axis of the pressure curve. When setting seven sampling points, an obvious error (about 25%) appears in the curve axis, and the error decreases with the increase of radial distance. Because the deflection angle gradient is input in Abel inverse equation, reconstruction error is more likely to occur in the area with the most significant deflection angle gradient. For this reason, this paper adds a sampling point at 0.05 in the radial position. When using these eight sampling points for pressure reconstruction, it can be seen from Figure 10 that the reconstruction error at the axis reduces within 5%. When the radial coordinate is greater than 0.04, the reconstruction error is less than 1%.

It can be seen from Figure 8-10 with the corresponding analysis that the pressure reconstruction method in the corona discharge region proposed in this paper performs well when the deflection angle sampling points are sufficient. Through analysis, the source of reconstruction error is the number of sampling points, especially in regions with large deflection angle gradients. Its reconstruction error is susceptible to the number of sampling points. In order to improve the accuracy of pressure field reconstruction, on the one hand, the spatial resolution of the Schlieren image should be improved at the hardware level. On the other hand, the original image should be pre-processed at the software level using appropriate interpolation techniques.

IV. RELATIONSHIP BETWEEN PRESSURE FIELD AND AUDIBLE NOISE OF DC CORONA DISCHARGE

A. THE MEASUREMENT PLATFORM FOR SCHLIEREN IMAGE AND SOUND PRESSURE

A time domain synchronous measurement platform was setup to measure the pressure field and audible noise of DC corona discharge, as shown in figure 11.

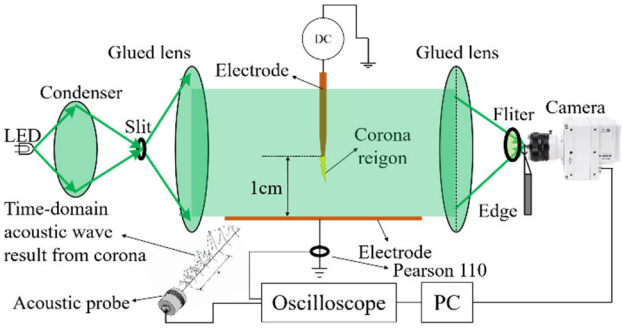

FIGURE 11. The measurement platform for schlieren image and sound pressure.

The measurement platform contains:

(1) The DC source consists of a 50 Hz AC transformer with partial discharge <5 pC), a high-voltage rectifier silicon stack, and a high-voltage capacitor of 1.668 μF. The DC voltage ripple coefficient is 1% when the corona current increases to 100 mA, which meats the high voltage DC test requirement.

(2) The Schlieren optical system includes the LED light source with wavelength of 532 nm, a condenser lens with focal length of 15cm, a pair of glued lenses (focal length: 25cm), a sharp knife, and a filter with the optical transmission wavelength of 532nm. The diameter of all the lens is 4cm.

(3) The Schlieren image is capture by a Phantom V710Ls high-speed camera, the spatiotemporal resolution of the Schlieren image is 38.45 μs and 100 μm/pixel.

(4) The corona current is measured by a Pearson current monitor model 110, with a conversion ratio of 0.1 mV -1 mA, a minimum sampling frequency of 1 kHz, and a maximum sampling frequency of 20 MHz.

(5) The audible noise measurement system contains an AWA14423 1/2 inch microphone from Aihua Company with a nominal sensitivity of 50 mV/Pa, the frequency range is 10-2000 Hz, and the dynamic range is 17-140 dB; an AWA14604 preamplifier with a frequency response of $\pm$ 0.1 dB in the 20 Hz to 20 kHz measurement range, the transmission gain is -0.1 dB, and the background noise is less than 5 μV; an AH6012 front power supply box with a transmission gain of 0 dB.

(6) The measured sound pressure and current are collected by a Teledyne HDO6104A oscilloscope, with a vertical resolution of 12 bits, four sampling channels, the maximum sampling rate is 10 GSa/S, the bandwidth is 1 GHz, and the typical background noise value is 18 μV.

B. RESULTS AND DISCUSSION

Figure 12 shows the Schlieren image and current from the corona to spark discharge within a 1cm needle-plate gap.

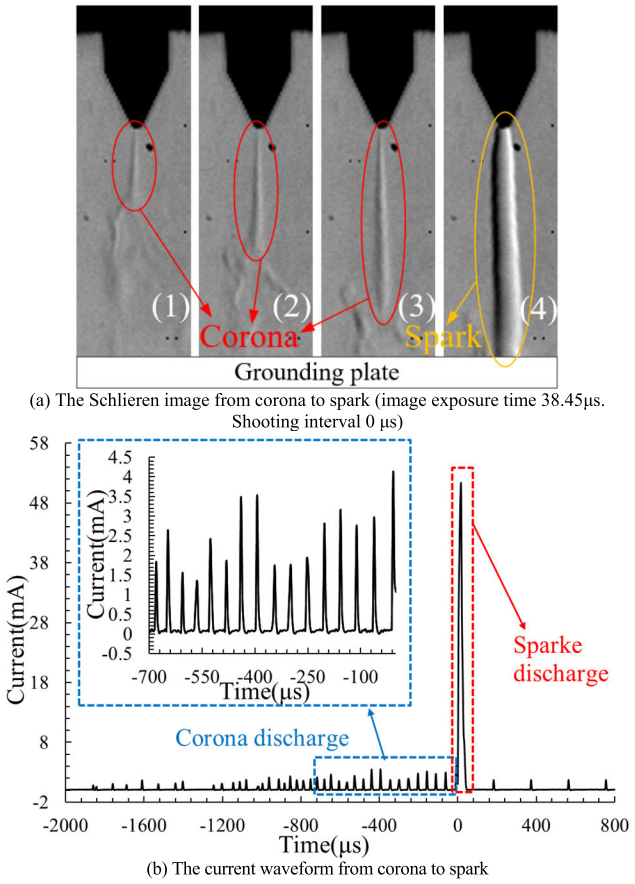

(a) The Schlieren image from corona to spark (image exposure time 38.45μs. Shooting interval 0 μs)

(b) The current waveform from corona to spark

FIGURE 12. The Schlieren image and current from corona to spark discharge.

In figure 12 (a), the red circle and arrows marked the corona region, the yellow circle and arrow marked the spark region. In figure 12 (b), the blue and red dotted lines marked the corona and spark discharge waveform, respectively. The zero time of the current waveform was set when the current jump appears that represents the spark discharge appears. It can be seen from the figure that:

(1) The corona region generated from the needle electrode can be observed and then expanded to the ground plate, forming the spark discharge. It can be seen from the sub-images (figure a 1∼4) that the discharge regions in different discharge stages are very different in shape and size. During the corona discharge, the length of the corona region develops within the needle-plate gap, when the corona region developed to the grounding plate, the spark discharge appears with larger radius and more prominent discharge channel.

(2) Higher current amplitude appears when the spark discharge formed. From the figure 12 (b), it can be seen that the amplitude of corona current maintains at several mill-ampere, and the amplitude of current jump to tens of mill-ampere when the discharge region bridged the gap (figure 12 a 4), compared with the significant changes in the morphology of the discharge region.

This paper uses the proposed image processing and pressure reconstruction methods to reconstruct the pressure distribution of the four sub-images in the figure 12 (a). Results are shown in the figure 13.

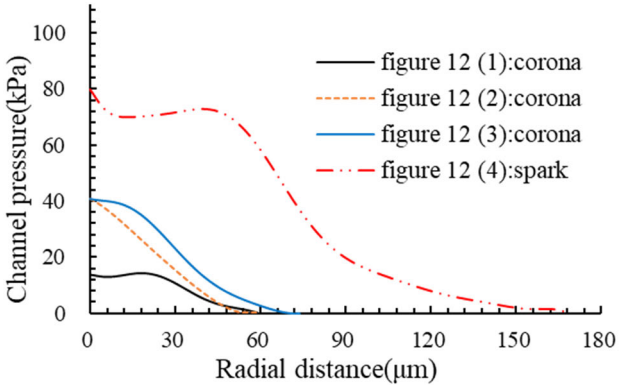

FIGURE 13. Channel pressure reconstruction results.

As shown in Figure 13, the pressure field in the discharge region at different discharge stages from corona to spark can be obtained in a smooth and continuous form using the proposed method. Within figure 13, it can be seen that:

(1) The Schlieren system captures the discharge channel's pressure recovery and gas expansion process at the microsecond scale. According to the existing electroacoustic theory, the sound generation process is that the gas compression in the discharge area forms a positive half-wave of the sound wave. The gas expansion forms a negative half-wave of the sound wave. The measured pressure in Figure 13 is less than the ambient pressure, which is the discharge channel's pressure recovery and gas expansion process.

(2) The radial radius of the discharge channel increases continuously from the corona to spark discharge under DC voltage. The corresponding radial radii of the four curves in Figure 12 (a) are 59.5 μm, 60 μm, 76 μm, and 168 μm, respectively.

(3) Under DC voltage, the over pressure P_{dgas} increases from the corona to spark discharge. The pressure amplitudes corresponding to curves (1), (2), (3), and (4) are 13.6 kPa, 40.63 kPa, 40.8 kPa, and 79.6 kPa, respectively.

Figure 14 shows the typical time domain waveform of DC corona discharge; from the figure, it can be seen that:

(1) The sound pressure waveform is a two-polarity wave, which is the same as existing papers [33], [34]. Figures 14 (a) and (b) present that the sound wave generated

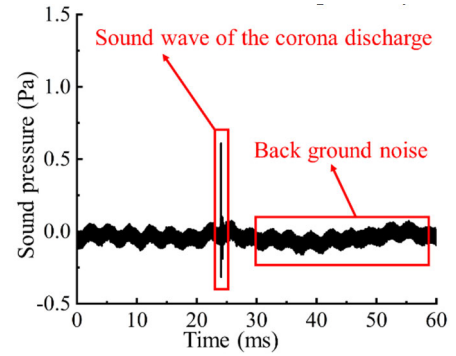

(a) The sound wave and back ground noise

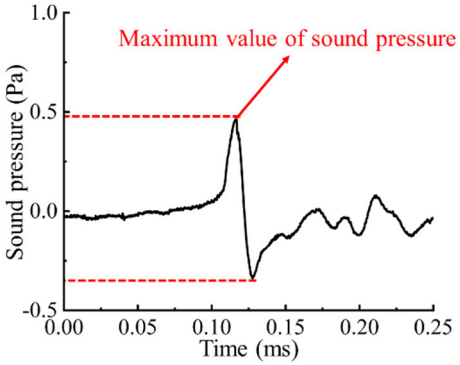

(b) The waveform of DC corona discharge

FIGURE 14. Sound wave generates from the DC corona discharge.

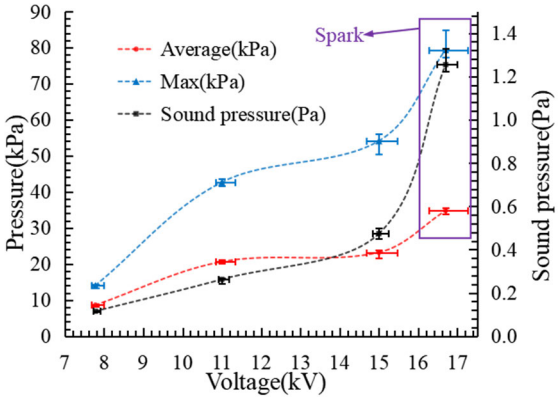

(a)The pressure from corona to spark

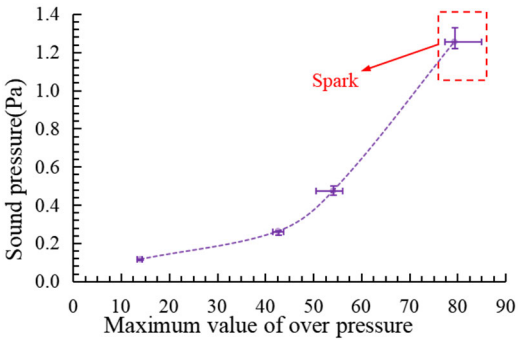

(b)The relationship between sound pressure and over pressure

FIGURE 15. The relationship between sound pressure and over pressure within corona discharge.

from corona discharge contains positive and negative half waves; the maximum sound pressure value is the absolute value of the two polarities. Figure 14 (b) shows that the maximum value is about 0.495 Pa at the positive half wave.

(2) The maximum value of the positive half is higher than the negative half of the sound pressure wave. In Figure 14(a) and (b), it is obvious that the positive half is bigger than the negative half. The amplitude of the positive half is 0.7 Pa and 0.495 Pa in figure 14 (a) and (b). The amplitude of the negative half is -0.4 Pa and -0.38 Pa in Figures (a) and (b), which is less than the positive half.

(3) The sound wave is obvious compared with the background noise. As shown in figure 14 (a), the background noise fluctuates between ±0.1 Pa, where the amplitude value is around 0.38∼0.5 Pa, and the signal-to-noise ratio is around 3.8∼5.

This paper studied the pressure flied characteristics and its relationship with sound pressure using the test platform, main results are shown in the figure 15 and table 1.

TABLE 1. Experiment results of the different discharge stage.

Discharge stage	Corona	Corona	Corona	Spark
Voltage(kV)	7.78	11	15	16.7
Max(kPa)	14.05	42.64	54.11	79.35
Average(kPa)	8.62	20.61	23.20	34.75
Sound pressure(kPa)	0.12	0.26	0.47	1.25

Figure 15 (a) shows the pressure's max value (blue triangle), average value (red circle), and the sound pressure (black square) under different DC voltage. Figure 15 (b) shows the relationship between sound pressure and the maximum value of the over pressure within the discharge region. Table 1 gives the data that contains in the figure 15 (a). In figure 15 the results from spark discharge was highlighted using a square frame. It can be seen that:

(1) The pressure field and sound pressure increase from the corona to spark discharge. In Figure 15 (a), from corona to spark discharge, the pressure field's max value and average value increase from 14.05 kPa to 79.35 kPa, and 8.62 kPa to 34.75 kPa, respectively; the sound pressure increase from 0.12 Pa to 1.25 Pa.

(2) A relationship of nonlinear proportional increase is discovered between sound pressure and the pressure field. In Figure 15 (b), the sound pressure increase from 0.1 Pa to 1.25 Pa with the max value of the pressure field. However, the relationship between them is nonlinear.

(3) The pressure characteristics in the corona region shows a saturation trend, and the pressure field is significantly increased after the corona turns into a spark discharge. When the voltage increase from 7.78 kV to 11 kV and 11 kV to 15 kV, the max value of pressure increased 28.59 kPa and 11.47 kPa, the average value increased 11.99 kPa and 2.59 kPa, respectively. However, when the corona turns to

spark, the max and average value of pressure increased 25.24 kPa and 11.55 kPa.

(4) A small portion of the pressure field's pressure is converted into sound pressure during corona discharge. Compared with the value of the pressure field and sound pressure, it is obvious that the pressure field locates at the kPa level, and the sound is only in Pa. The pressure field is about a thousand times larger than sound pressure.

V. CONCLUSION

This paper introduces the DC corona discharge's image processing and pressure field reconstruction methods and the relationship between pressure field and sound pressure. The results demonstrated an effective way to measure and analyze the pressure field in the region of DC corona discharge. The following main conclusions are drawn:

(1) The corona discharge region has a smaller geometrical size, a more stable region shape, and fewer sampling points than the spark discharge. The discharge area of spark discharge has a larger geometric size, an unstable region, and more sampling points than the corona. The comparison between various image processing methods showed that bicubic interpolation could be used for image pre-processing of corona discharge. For the spark discharge area, interpolation is unnecessary to avoid numerical errors.

(2) This paper's pressure field reconstruction method has good numerical calculation accuracy. The reconstruction error is within 0.7% when the sampling points are sufficient. The reconstruction error of the pressure field is caused by the lack of sampling points (especially the axis position) in the discharge area. When the sampling points are insufficient, three sampling points near the axis of the discharge area can maintain the reconstruction error within 5%. The Schlieren system can capture the discharge channel's pressure recovery and gas expansion process at the microsecond timescale. From DC corona to spark discharge, the radial radius of the discharge region increases, and the pressure amplitude decreases.

(3) The pressure field and sound pressure increase from corona to spark discharge; a relationship of nonlinear proportional increase appears between the pressure field and audible noise (quantified in sound pressure). Results show that only a small portion of the pressure field is converted into sound pressure during corona discharge.

ACKNOWLEDGMENT

This work was supported by Electric Power Research Institute of Guangdong Power Grid Co., Ltd., Grant Agreement No 036100KK52200034(GDKJXM20201968).

REFERENCES

[1] Y. Yang, H. Chen, C. Li, H. Zhang, Z. Yu, C. Li, S. Yang, and X. Pi, "Comparison of initiation and temporal evolution of positive and negative ionic wind under needle-to-plate electrode," *IEEE Trans. Plasma Sci.*, vol. 51, no. 2, pp. 352–358, Feb. 2023, doi: 10.1109/TPS.2023.3239781.

[2] C. Jing, W. Xiaowen, and C. Hao, "Anti-burst intermittent environmental interferencedetection technology of transformer noise," *Guangdong Electr. Power*, vol. 35, no. 8, pp. 113–121, 2022.

[3] Li Xiaojuan, M. Huan, Li Shaoyu, C. Bibo, J. Jin, and L. Wenhui, "Influence of electric field in transformer area of 500 kV substation on human body," *GUANGDONG Electr. POWER*, vol. 35, no. 2, pp. 121–127, 2022.

[4] Y. Liu, Z. Li, Z. Qin, X. Li, Y. Liu, H. Huang, and F. Huang, "Research on the simulation method for HVDC continuous positive corona discharge," *IEEE Trans. Plasma Sci.*, vol. 50, no. 9, pp. 2805–2814, Sep. 2022, doi: 10.1109/TPS.2022.3196038.

[5] S. Hedtke, P. Bleuler, and C. M. Franck, "Outdoor investigation of the corona characteristics and audible noise of a hybrid AC/DC overhead line," *IEEE Trans. Power Del.*, vol. 36, no. 6, pp. 3309–3317, Dec. 2021, doi: 10.1109/TPWRD.2020.3038414.

[6] K. Yoshida, T. Hoshino, S. Murase, H. Murakami, and T. Miyashita, "Analysis of load noise components in small core-form transformers," *IEEE Trans. Power Del.*, vol. 36, no. 5, pp. 2694–2704, Oct. 2021, doi: 10.1109/TPWRD.2020.3025816.

[7] Z. Hailan, *Theoretical Acoustics*. Beijing, China: Higher Educ. Press, 2007.

[8] Q. Li, Y. Li, S. Rowland, J. Hu, I. Cotton, and X. Jiang, "Audible noise evaluation for six-phase overhead lines transformed from existing three-phase double circuit infrastructures with uprated voltages," *High Voltage*, vol. 7, no. 5, pp. 866–876, Oct. 2022.

[9] Q. Li, S. M. Rowland, I. Dupere, and R. S. Morris, "The impact of water droplet vibration on corona inception on conductors under 50 Hz AC fields," *IEEE Trans. Power Del.*, vol. 33, no. 5, pp. 2428–2436, Oct. 2018.

[10] Q. Li, S. M. Rowland, I. Dupere, and R. Shuttleworth, "Acoustic noise evaluation for overhead line conductors using an anechoic chamber," *IEEE Trans. Power Del.*, vol. 32, no. 4, pp. 1835–1843, Aug. 2017.

[11] Q. Li, R. Shuttleworth, G. Zhang, I. Dupere, and S. M. Rowland, "Acoustic noise evaluation for overhead line conductors," in *Proc. IEEE Electr. Insul. Conf. (EIC)*, Ottawa, ON, Canada, Jun. 2013, pp. 119–123, doi: 10.1109/EIC.2013.6554216.

[12] G. He, Q. Hu, L. Shu, X. Jiang, H. Yang, D. Yang, and R. Sundararajan, "Impact of icing severity on positive corona generated audible noise characteristic of rime ice-covered conductor," *IEEE Trans. Ind. Appl.*, vol. 55, no. 5, pp. 5269–5276, Sep. 2019.

[13] Y. Liu, Y. Liu, H. Yuan, and L. Ji, "Research on the correlation between the frequency-domain characteristics of corona current and A-weighted sound level of audible noise for UHV DC transmission line," *IET Gener., Transmiss. Distrib.*, vol. 12, no. 11, pp. 2549–2556, Jun. 2018.

[14] Li Xuebao, C. Xiang, and L. Tiebing, "Experimental studies on the time-domain characteristics of audible noise from single corona source on the conductor under DC voltage," *Proc. CSEE*, vol. 34, no. 24, pp. 4152–4160, 2014.

[15] B. Zhang, Z. Li, and J. He, "A numerical model of acoustic wave caused by a single positive corona source," *Phys. Plasmas*, vol. 24, no. 10, Oct. 2017, Art. no. 103521.

[16] Li Xuebao, "Time-domain characteristics and calculation model of corona-generated audible noise on DC conductors," Doctor Thesis, Dept. Elect. Eng., North China Electr. Power Univ., Beijing, China, 2016.

[17] Li Xuebao, C. Xiang, and L. Tiebing, "Analysis and fitting of the time-domain waveform of the audible noise caused by single positive corona source on the conductor," *Power. Syst. Tech.*, vol. 38, no. 6, pp. 150–157, 2014.

[18] Y. P. Raizer, *Gas Discharge Physics*. Oxford, U.K.: Springer, 1991.

[19] Y. Yue, Y. Zou, H. Wang, F. Huang, and C. Wang, "Research on observation method of leader discharge thermal expansion based on quantitative Schlieren technique," *IOP Conf. Ser., Earth Environ. Sci.*, vol. 310, no. 3, Aug. 2019, Art. no. 032059.

[20] Q. Xiong, L. Xu, X. Wang, L. Xiong, Q. Huang, Q. Chen, J. Wang, W. Peng, and J. Li, "Full spatial-field visualization of gas temperature in an air micro-glow discharge by calibrated Schlieren photography," *J. Phys. D, Appl. Phys.*, vol. 51, no. 9, Mar. 2018, Art. no. 095207.

[21] R. Ono and T. Oda, "Visualization of streamer channels and shock waves generated by positive pulsed corona discharge using laser Schlieren method," *Japanese J. Appl. Phys.*, vol. 43, no. 1, pp. 321–327, Jan. 2004.

[22] X. Zhao, L. Liu, Y. Yue, H. He, L. Liu, and J. He, "On the use of quantitative Schlieren techniques in temperature measurement of leader discharge channels," *Plasma Sources Sci. Technol.*, vol. 28, no. 7, Jul. 2019, Art. no. 075012.

[23] M. Wei, J. Hu, X. Wang, X. Jiang, R. Zhang, and L. Shu, "Experimental study on thermal characteristics of DC arc formation between ice-electrode gap," *IEEE Trans. Dielectr. Electr. Insul.*, vol. 28, no. 5, pp. 1497–1505, Oct. 2021.

[24] J. Hu, W. Meng, X. Wang, R. Zhang, K. Sun, and X. Jiang, "Expansion characteristics of a discharge column in an electrode–ice gap," *Phys. Plasmas*, vol. 28, no. 12, pp. 1–12, Dec. 2021.

[25] M. Wei, J. Hu, R. Zhang, X. Jiang, K. Sun, and X. Wang, "Study on the path and thermal characteristics of the spark discharge between ice and electrode gap," *IEEE Trans. Dielectr. Electr. Insul.*, vol. 30, no. 2, pp. 491–500, Apr. 2023, doi: 10.1109/TDEI.2023.3243617.

[26] Y. He, J. Wang, X. Chen, H. Miao, Y. Wu, and Z. Zhang, "Experimental study on characteristics of plasma synthetic jet actuators with different insulating materials," *IEEE Trans. Plasma Sci.*, vol. 50, no. 10, pp. 3583–3592, Oct. 2022, doi: 10.1109/TPS.2022.3201638.

[27] S. Shen, Q. Liu, and Z. Wang, "Shockwave characteristics of streamer propagation in insulating liquids under positive lightning impulse," *IEEE Trans. Dielectr. Electr. Insul.*, vol. 28, no. 2, pp. 493–501, Apr. 2021, doi: 10.1109/TDEI.2020.009238.

[28] M. Ghasemi, S. Yu, and M. H. Qaisrani, "Dynamics of the effluent gas turbulent front of the plasma jet driven by dual sources of a pulsed DC and AC power: Experimental study," *IEEE Trans. Plasma Sci.*, vol. 48, no. 9, pp. 3160–3167, Sep. 2020, doi: 10.1109/TPS.2020.3015696.

[29] Y. Cui, C. Zhuang, X. Zhou, R. Zeng, and J. He, "Thermodynamic properties of negative discharge channels in a 1-m air gap measured by optical interferometry," *IEEE Trans. Plasma Sci.*, vol. 47, no. 5, pp. 1917–1925, May 2019.

[30] I. Gallimberti, "The mechanism of the long spark formation," *Le J. Phys. Colloques*, vol. 40, no. C7, pp. C7-193–C7-250, Jul. 1979.

[31] K. Tsuda, K. Takahashi, and K. Satoh, "Visualizing spatiotemporal temperature variation for estimating H_{aq}^{+} distribution by pulsed discharge plasma exposure," *IEEE Trans. Plasma Sci.*, vol. 49, no. 5, pp. 1739–1744, May 2021, doi: 10.1109/TPS.2021.3069540.

[32] E. M. Dianov, V. E. Fortov, I. A. Bufetov, V. P. Efremov, A. E. Rakitin, M. A. Melkumov, M. I. Kulish, and A. A. Frolov, "High-speed photography, spectra, and temperature of optical discharge in silica-based fibers," *IEEE Photon. Technol. Lett.*, vol. 18, no. 6, pp. 752–754, Mar. 15, 2006, doi: 10.1109/LPT.2006.871110.

[33] X. Li, X. Cui, T. Lu, D. Wang, W. Ma, and X. Bian, "Comparison between the audible noises generated from single corona source under DC and AC corona discharge," *CSEE J. Power Energy Syst.*, vol. 1, no. 3, pp. 23–30, Sep. 2015, doi: 10.17775/CSEEJPES.2015.00031.

[34] C. Ren, J. Wang, P. Yan, R. Xu, and T. Wang, "Polarity effect on corona discharge of needle-plane electrodes and audible noise under DC voltage," in *Proc. IEEE 11th Int. Conf. Properties Appl. Dielectr. Mater. (ICPADM)*, Sydney, NSW, Australia, Jul. 2015, pp. 784–787, doi: 10.1109/ICPADM.2015.7295389.

MENG WEI was born in Yunnan, China, in June 1994. He received the bachelor's and Ph.D. degrees from Chongqing University, Chongqing, China, in 2016 and 2022, respectively. He is currently a Postdoctoral Researcher with Chongqing University and the Electric Power Research Institute, Guangdong Power Grid Company Ltd. His main research interests include gas discharge plasma, insulation coordination for transmission lines, and electromagnetic environment for transmission lines.

LI LI was born in Hubei, China, in August 1971. She has working at the Key Laboratory of Environmental Protection of Guangdong Power Grid Company Ltd., Electric Power Research Institute of Guangdong Power Grid Company Ltd., as the professorate senior engineer for more than 20 years, and currently she is the Vice-Chief Engineer of the China Southern Power Grid and Key Laboratory of Environmental Protection of Guangdong Power Grid Company Ltd. She is currently the Vice-Chief Engineer of China Southern Power Grid. She has led wide range of research projects in electromagnetic environmental emissions from power equipment, advanced methods for environmental protection in power systems, and the carbon emission reduction of the power equipment. She has published four books, 24 technical invention patents, and over 60 papers. In recent years, she is an Active Member of the CIGRE Working Group B2.69; and a Committee Member of the China Occupational Safety and the Health Association Noise, the Vibration Control Committee, the Power Industry Environmental Protection Standard Committee, and the Power Grid Electromagnetic and Noise Control Standard Committee. As the main contributor, she has won twice the China Patent Excellence Award and nine times the Ministerial and Provincial-Level Science and Technology Awards.

LI QI (AKA STEVEN) was born in Hunan, China, in September 1984. He received the B.Eng. degree in electrical and electronics engineering from the University of Birmingham and the Huazhong University of Science and Technology, in 2007, and the M.Sc. (Hons.) and Ph.D. degrees in electrical power engineering from The University of Manchester, in 2009 and 2013, respectively. Since then, he has been with The University of Manchester, the National Grid U.K., and Chongqing University (China) for nine years before joining The University of Manchester, as a Dame Kathleen Ollerenshaw Fellowship. Within academia and industry, he has led around 20 research projects with wide range of topics for power industry. His research interests include reliability for solid dielectrics, advanced UHV/EHV electricity transmission line optimization for future net-zero power systems, electromagnetic environmental emissions from UHV/EHV transmission lines, and the application of artificial intelligent into future power systems. He is an Active Member of the CIGRE Working Group B2.69 and B2.83 and a Youth Committee Member of the China Electrotechnical Society. He was one of the recipients of the IET Innovation Award, in 2015.

LI DUANJIAO was born in 1971. She is a Senior Engineer of Guangdong Power Grid Company Ltd. Her main research area is the insulation and online monitoring of high-voltage power equipment.

HU JIANLIN (Member, IEEE) was born in Hubei, China, in 1978. He received the M.Sc. and Ph.D. degrees from Chongqing University, Chongqing, China, in 2003 and 2009, respectively. He is currently a Professor with the School of Electrical Engineering, Chongqing University. His main research interests include high voltage external insulation, discharge phenomenon in outdoor insulators, and insulation coordination for transmission lines.

WANG HONGBIN was born in 1972. He is a Senior Engineer of Guangzhou Power Supply Bureau, Guangdong Power Grid Company Ltd. His main research interests include high voltage and insulation technology, smart grid technology, and power robots.

ZHENG XIAOGUANG was born in 1966. He is a Senior Engineer of the Electric Power Research Institute, Guangdong Power Grid Company Ltd. His main research area is the high voltage and insulation technology.

ZHONG WANLI was born in 1968. He is a Senior Engineer of the Electric Power Research Institute, Guangdong Power Grid Company Ltd. His main research interests include the supervision of metal technology and prevention and control of transmission line disasters.